Journal of Biomedical Optics

SPIEDigitalLibrary.org/jbo

Dual-tracer background subtraction approach for fluorescent molecular tomography

Kenneth M. Tichauer
Robert W. Holt
Fadi El-Ghussein
Scott C. Davis
Kimberley S. Samkoe
Jason R. Gunn
Frederic Leblond
Brian W. Pogue

SPIE

Dual-tracer background subtraction approach for fluorescent molecular tomography

Kenneth M. Tichauer,[a] Robert W. Holt,[b] Fadi El-Ghussein,[a] Scott C. Davis,[a] Kimberley S. Samkoe,[c] Jason R. Gunn,[a] Frederic Leblond,[a,d] and Brian W. Pogue[a,b,c]
[a]Dartmouth College, Thayer School of Engineering, Hanover, New Hampshire 03755
[b]Dartmouth College, Department of Physics and Astronomy, Hanover, New Hampshire 03755
[c]Dartmouth Medical School, Department of Surgery, Lebanon, New Hampshire 03756
[d]ÉcolePolytechnique Montréal, Génie Physique, Montréal, Quebec H3C 3A7, Canada

Abstract. Diffuse fluorescence tomography requires high contrast-to-background ratios to accurately reconstruct inclusions of interest. This is a problem when imaging the uptake of fluorescently labeled molecularly targeted tracers in tissue, which can result in high levels of heterogeneously distributed background uptake. We present a dual-tracer background subtraction approach, wherein signal from the uptake of an untargeted tracer is subtracted from targeted tracer signal prior to image reconstruction, resulting in maps of targeted tracer binding. The approach is demonstrated in simulations, a phantom study, and in a mouse glioma imaging study, demonstrating substantial improvement over conventional and homogenous background subtraction image reconstruction approaches. [DOI: 10.1117/1.JBO.18.1.016003]

Keywords: image reconstruction; cancer; targeted imaging agent; small animal.

Paper 12673 received Oct. 10, 2012; revised manuscript received Nov. 27, 2012; accepted for publication Nov. 30, 2012; published online Jan. 4, 2013.

1 Introduction

Fluorescence tomography (FT) is a promising molecular imaging modality that is capable of mapping biomolecule distributions in tissue without requiring the use of ionizing radiation, such as is required in competing nuclear medicine modalities. However, while FT is very sensitive, the propagation of light through tissue is hindered by a significantly greater amount of scattering and absorption than ionizing radiation (e.g., x-rays), limiting the depth of tissue that can be imaged through to several centimeters.[1] This depth limitation has restricted applications of whole-body FT to small animal imaging to date, where it has shown great promise as a preclinical tool for *in vivo* investigations of biomolecular pathways in disease states.[2] This study introduces an approach to doing diffuse FT that has some inherent benefits in image reconstruction accuracy, as well as peripheral benefits by allowing imaging of molecular binding at very short times after contrast injection *in vivo*.

Contrast in FT is typically based on the injection of a fluorescently labeled molecular drug that will preferentially bind to a specific biomolecule of interest (e.g., cellular receptors that are over-expressed in pathological processes). Immediately after injection, the tracer is dispersed throughout the body and over time it is cleared from the plasma and tissues that are devoid of the biomolecule of interest. It is retained in areas where it has bound to the targeted biomolecule, thus providing fluorescent contrast only in tissues where the receptor is 'over-expressed.' The strength of this approach is that the targeted molecule can be synthesized to bind most biomolecules of interest, and as long as the chosen biomolecule is in a region that can be accessed by the tracer, the approach should be practicable. The problem with the approach is that at early timepoints there can be significant levels of background tracer uptake,[3] and by waiting the hours or even days necessary for the background to dissipate, it is more likely for effects, such as cellular internalization or metabolism of the tracer, to affect the relationship between fluorescence and receptor density.[4] Furthermore, at these extended time points there may still be considerable nonspecific tracer concentrations in organs of filtration like the liver, kidneys, spleen, and bladder, confounding the ability to localize bound fractions of the tracer, at least in the abdomen.[5] This study develops one new approach toward advancing this area.

The nonlinearity of image reconstruction algorithms in FT make background fluorescence severely detrimental to resolving bound tracer populations of interest.[6] In response, a number of approaches have been designed to mitigate the effects of background: such as constraint-based reconstruction algorithms,[7–11] spectral and lifetime removal of autofluorescence,[12–14] preinjection image subtraction,[15] and analytical modeling of background fluorescence.[6,16,17] However, while many of these approaches work well for autofluorescence removal or removal of homogeneously distributed fluorescent backgrounds, they are not ideal if the background is heterogeneous and predominantly comprised of nonspecific fluorescent tracer uptake, which may be expected in molecularly targeted FT studies at earlier timepoints after targeted tracer injection.[18] In the present study, an approach is proposed wherein the uptake of a second, untargeted fluorescent tracer is used to subtract off the nonspecific uptake of a simultaneously injected targeted fluorescent tracer. As long as the two tracers have similar delivery characteristics (i.e., their vascular permeability), nonspecific uptake, and pharmacokinetics[19]—and the nonspecific fluorescence uptake is much greater than the level of autofluorescence[3]—the untargeted tracer fluorescence data can be used as a scaled surrogate of the unbound component of the targeted tracer uptake, allowing

Address all correspondence to: Brian W. Pogue, Dartmouth College, Thayer School of Engineering, Hanover, New Hampshire 03755. Tel: 603-646-3861; Fax: 603-646-3856; E-mail: Brian.W.Pogue@dartmouth.edu

a means of subtracting off the unbound (background) signal. The strength of this is that the approach is feasible even if the background is heterogeneous or is found in high concentrations in organs of filtration.[20] This development, originally proposed in a previous study,[21] is presented in detail in the current study and explored through simulations, phantom experiments, and in a pilot *in vivo* study.

2 Theory

2.1 *Dual-Tracer Background Subtraction*

When exciting fluorescent molecules within a biological tissue, the measurement of reemitted fluorescent light at the surface can be considered linear with respect to the fluorophore concentration in the limit that the absorption of the fluorophores is much less than that of the main endogenous absorbers in tissue (including hemoglobin, lipids and water).[22] The dual-tracer background subtraction approach introduced in this study assumes this linearity hypothesis holds at two wavelengths of interest, namely the excitation wavelengths of a targeted and an untargeted fluorescent tracer. The general mathematical framework for the single-wavelength linear FT inverse problem has been presented elsewhere,[23] and so here the methodology of a general dual-wavelength FT problem is set up and solved. If m optical measurements are made and the interrogated spatial domain is discretized into n volume elements (e.g., finite elements or rectilinear voxels), the linear problem can be expressed as a matrix equation mapping the n-by-1 fluorescence yield vector, x_i (where $i = T$ represents the notation for data from a targeted tracer and $i = U$ is notation for an untargeted tracer), to the m-by-1 data vector, d_i, composed of fluorescence measured at select source-detector pair positions on the surface of the imaging domain at targeted and untargeted tracer wavelengths, λ_i:

$$J_i x_i = d_i. \tag{1}$$

The operator J_i is the m-by-n forward model or sensitivity matrix defined at wavelengths λ_i. For a given imaging geometry and spatial discretization, and in the diffusion limit,[24] J_i is strictly a function of the light absorption (μ_a) and reduced scattering (μ_s') properties of the imaging medium. These properties vary amongst all n imaging domain elements and are included in the vector μ_i: i.e.,

$$J_i = J(\mu_i). \tag{2}$$

To understand the utility of the untargeted tracer distribution as a means of removing unwanted background signal from a targeted tracer distribution (and potentially other factors unaccounted for through modeling), the vectors x_T and x_U, representing the targeted and untargeted tracer distributions, respectively, can be expanded as follows:

$$\begin{aligned} x_T &= x_{\text{bound}} + x_{\text{bk}} + x_{\text{af}} \\ x_U &= x_{\text{bk},u} + x_{\text{af},u}, \end{aligned} \tag{3}$$

where the vector x_{bound} represents the amount of targeted fluorophore bound to its specific receptor at each element of the domain, the vector x_{bk} is the amount of unbound or 'background' targeted fluorescence at each element of the domain, the vector x_{af} is the amount of autofluorescence (endogenous fluorescence)[25] at the wavelength used to detect the targeted fluorescence, and the vectors $x_{\text{bk},u}$ and $x_{\text{af},u}$ are the corresponding background and autofluorescence distributions at the untargeted tracer wavelength. It should be noted that there is no *bound* term in x_U as a result of the untargeted tracer not being able to bind to the specific receptors of the targeted tracer.

If the simultaneously injected untargeted tracer (fluorescing at a different wavelength: typically >50 nm peak-to-peak separation) is assumed to have similar delivery characteristics to the targeted tracer, the background distribution of the targeted tracer can be approximated to be a linear function of the background distribution of the untargeted tracer. For example, mathematically this would be, $x_{\text{bk}} = c_1 x_{\text{bk},u}$, where c_1 is a constant that accounts for effects such as differences in the system sensitivity at the targeted and untargeted tracer wavelengths and/or differences in quantum efficiency or injected concentration between the two tracers. Similarly, a second hypothesis here is that the autofluorescence at the targeted tracer wavelength can be written as a linear function of the autofluorescence at the untargeted tracer wavelength. This can be mathematically expressed as, $x_{\text{af}} = c_2 x_{\text{af},u}$, where c_2 is a constant that accounts for differences in the magnitude of autofluorescence at the targeted and untargeted tracer wavelengths. Therefore, Eq. (1) can be re-written at the targeted and untargeted tracer wavelengths as follows:

$$\begin{aligned} J_T(x_{\text{bound}} + x_{\text{bk}} + x_{\text{af}}) &= d_T \\ J_U\left(\tfrac{x_{\text{bk}}}{c_1} + \tfrac{x_{\text{af}}}{c_2}\right) &= d_U. \end{aligned} \tag{4}$$

In order to accommodate the forward model matrix difference, a third hypothesis is made that an 'average' sensitivity function, $\bar{J}$, can be defined as follows:

$$\bar{J} \equiv J(\bar{\mu}), \tag{5}$$

where $\bar{\mu}$ is the mean of the optical properties in the vectors μ_T and μ_U. This new sensitivity function is taken to have similar mathematic properties to the matrices J_T and J_U and is used henceforth. In addition, the fourth and last hypothesis is that $x_{\text{af}} \ll x_{\text{bk}}$ holds at both wavelengths, which is true for systemically injected near-infrared fluorescent tracers at least out to 24 h after injection.[3] If these four hypotheses are accurate, the difference of the two lines in Eq. (4) can be simplified to:

$$\bar{J} x_{\text{bound}} = d_T - c_1 d_U. \tag{6}$$

The scaling coefficient, c (redefined for brevity from c_1), is difficult to calculate directly because the quantum efficiencies of the two fluorophores are difficult to know exactly and the sensitivity of the imaging system as a function of wavelength is difficult to characterize. Instead, since most targeted FT applications assume binding will occur only within a set number of inclusions within the imaging domain, it is assumed that for some source-detector pair the relative contribution of bound targeted signal to d_T will be negligible.[6,17] Assuming this, c can be estimated in the following way:

1. Find c_0 such that $\max(c_0 d_U) \leq 0.1 * \min(d_T)$.
2. Define $d_{U,\text{test}} = 1.01^p c_0 d_U$, where p is a positive integer.
3. Find maximum p such that $\min(d_T - d_{U,\text{test}}) > 0$.
4. Take $c = 1.01^p c_0$.

Thus a method is provided to build all parts of Eq. (6), save the unknown bound distribution, which is the quantity of interest.

2.2 *Homogeneous Background Subtraction*

If the background fluorescence is assumed to be relatively homogeneous, then it may not be necessary to employ a second untargeted tracer for the background subtraction.[17] Rather, homogeneous fluorescence background can potentially be removed by substituting a simulated Born-normalized data vector that assumes some level of homogenous fluorescence dispersed throughout the imaging domain in place of d_U in Eq. (6). Henceforth this approach will be referred to as the homogeneous background subtraction approach.

3 Methods

3.1 *Simulations*

To test the validity of the dual-tracer background subtraction approach, two simulation studies were carried out. In the first, the ability to locate a fluorescent inclusion in the presence of increasing background (while not changing the contrast in the inclusion) was investigated. Data were created from forward model simulations on a 25-mm diameter two-dimensional (2-D) circular mesh with 1521 nodes corresponding to 2496 triangular elements, carried out using the open-source software, NIRFAST (nirfast.org).[26] Within the mesh, two 5-mm diameter inclusions were simulated near half radii, separated by 90 deg [Fig. 1(a)]. Ten simulated datasets were created for fluorescent background levels, μ_f, ranging from 0 to 10^{-6} mm^{-1}, keeping a constant contrast level of 10^{-6} mm^{-1} (i.e., the fluorescence in the inclusions minus the fluorescence in the background was kept at a steady 10^{-6} mm^{-1} level). This corresponded to a contrast-to-background ratio (CBR) series ranging from infinite to unity. To make the simulation as realistic as possible, the absorption and reduced scattering coefficients were set to $\mu_a = 0.0182$ mm^{-1} and $\mu_s' = 1.08$ mm^{-1} at the excitation wavelength, and $\mu_a = 0.0164$ mm^{-1} and $\mu_s' = 1.01$ mm^{-1} at the emission wavelength of the simulated fluorophore. Fluorescence and transmittance data were simulated at 320 source-detector pairs about the mesh based on the geometry of the imaging system discussed in the following section. A 1% level of Gaussian noise was added to both the fluorescence and the transmittance datasets before ratioing the vectors to produce simulated Born-normalized datasets, the Born ratio being a format routinely used in FT because of its mitigating effects on model-data mismatch and a number of other approximations.[23] This level of noise is commensurate with the typical level of noise seen experimentally (results not shown).

Two approaches were employed to reconstruct fluorescence distribution from the first set of simulated Born ratio data using NIRFAST. Each employed an altered circular mesh with 1110 nodes and 2130 elements and a different set of assumed optical properties, $\mu_a = 0.0194$ mm^{-1} and $\mu_s' = 1.16$ mm^{-1} at the excitation wavelength, and $\mu_a = 0.0152$ mm^{-1} and $\mu_s' = 1.09$ mm^{-1} at the emission wavelength, to avoid inverse crimes and to account for the fact that experimentally, the optical properties cannot be known precisely. The first set of reconstructions was carried out by reconstructing directly on the product of the Born ratio data and a homogeneous forward model.[13] The second set of reconstructions was carried out using the homogreneous background subtraction approach (see Sec. 2). The same regularization parameter and stopping criterion were used for both approaches.

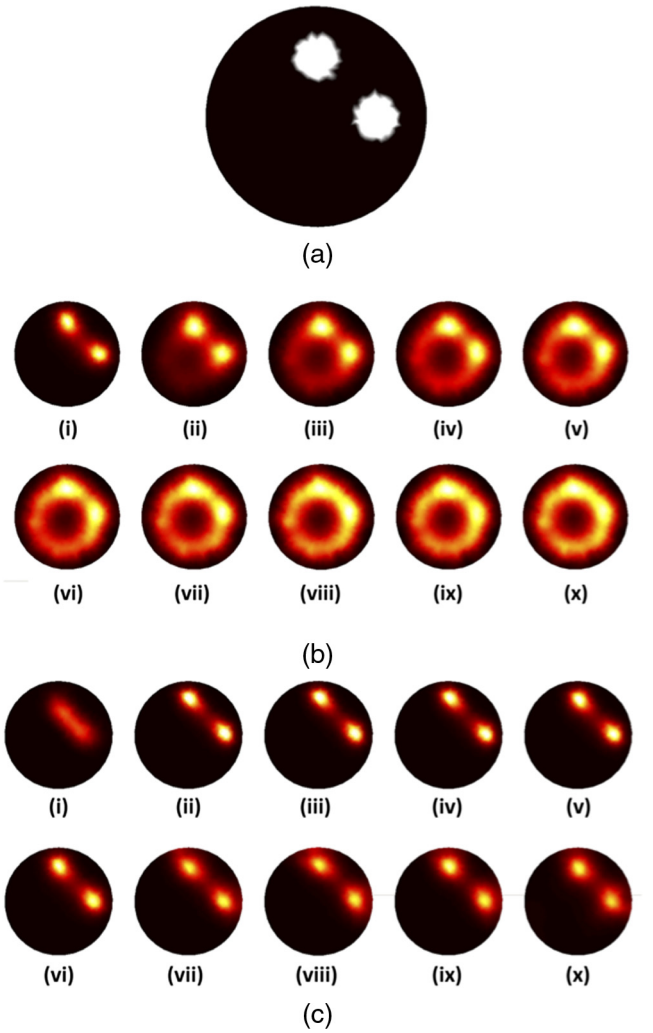

Fig. 1 Forward data were created based on a two-fluorescent inclusion circular mesh, shown in (a). Reconstructed fluorescence distributions resulting from increasing the level of background fluorescence while keeping the contrast of the inclusion over the background the same are presented in (b), (i)–(x). Each increment in Roman numeral corresponds to an increase in the background of 10% of the contrast, providing a range of contrast-to-background ratios ranging from infinity to unity. Reconstructions based on the data in (b) using the homogeneous background subtraction approach are presented in (c) (i)–(x).

In the second simulation study, two separate forward datasets were produced to approximate the uptake distribution of both a targeted and untargeted tracer. The targeted tracer forward data were produced from the identical mesh as in the first simulation (i.e., same mesh density, optical properties, and source-detector locations), but were constructed with an inhomogeneous background. The absorption due to fluorescence inside the inclusions was kept at 4×10^{-6} mm^{-1}, while a spatially modulated level of background fluorescence, ranging from 0 and 2×10^{-6} mm^{-1}, was created in a 2-D sinusoidal pattern with a periodicity of 10 mm [Fig. 2(a)], providing a mean tumor-to-background ratio of 4:1. The untargeted tracer forward data were produced on the same mesh again, with the heterogeneous background added, but with no inclusion [assuming no bound component, see Fig. 2(b)], and using optical properties that were 10% greater

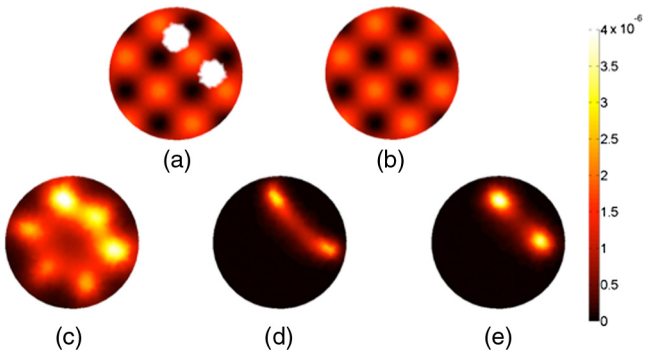

Fig. 2 Forward data were simulated on the fluorescence maps shown in (a) and (b), representing the distribution of a targeted and untargeted tracer, respectively. Reconstruction based only on data from (a) is shown in (c), reconstruction on data from (a) using the homogenous background subtraction is shown in (d), and reconstruction using the dual-tracer background subtraction on data sets from (a) and (b) is shown in (e).

than for the targeted tracer to approximate differences in absorption and scatter to be expected at the different wavelengths of the tracers. Born ratio data was produced from these meshes in the same manner as in the first set of simulations after 1% Gaussian noise was added to the raw fluorescence and transmittance datasets.

Three different reconstructions were carried out on these heterogeneous background data, all using the same reconstruction mesh with the same slightly erroneous optical properties described in the first simulation study. The first was a naïve approach, reconstructing on the raw targeted tracer Born ratio data alone. The second approach was the same homogeneous background-subtract approach carried out on the first set of simulated data. The final was the full dual-tracer approach characterized by Eq. (6), where the simulated targeted tracer data were substituted for d_T and the simulated untargeted tracer data were substituted for d_U. The same regularization parameter and stopping criterion were used in all cases and the reconstructions were performed with NIRFAST.

3.2 *Imaging System and Data Processing*

To test out the dual-tracer background subtraction approach in phantom and animal studies, fluorescence from targeted and untargeted fluorescent tracers was imaged on a micro-computed tomography-guided time-domain FT system. Much of the particulars of the system have been covered in depth previously,[27,28] however, some significant changes were made to the system to permit the simultaneous imaging of two fluorophores emitting at two different wavelengths. A schematic of the dual-wavelength version of the system is presented in Fig. 3(a). In brief, the FT system is a noncontact fan-beam geometry system using two pulsed-diode lasers (Picoquant, Berlin, Germany): one centered at 635 nm and the other centered at 755 nm. For the experiments carried out in this study, the lasers were pulsed at 40 MHz, 180 deg out of phase from each other. Each laser beam was passed through a 10-nm band-pass filter (Chroma Technologies, Bellows Falls, Vermont) centered at the respective wavelengths of the lasers, before both beams were coupled into separate 50-μm multimode optical fibers (Thorlabs, Newton, New Jersey). Tests of the laser demonstrated that the 755 nm laser was more powerful than the 635 nm laser, so as a means of having control over the relative strengths of the two lasers, the output of the 755-nm laser fiber was passed through an in-line motorized variable neutral density filter (OZ Optics, Ottawa, Ontario), before the optical fibers from both lasers were coupled together into a single 100-μm fiber using a custom-made fiber combiner (OZ Optics, Ottawa, Ontario). The output of the fiber combiner was then passed through a second variable neutral density filter to control the overall excitation power of the system, and then separated into two fibers using a 96/4 in-line beamsplitter (OZ Optics, Ottawa, Ontario). The 4% output was projected onto a reference photomultiplier tube (PMT, Hamamatsu Photonics, Japan) controlled by a time-correlated single photon counting (TCSPC) card (Becker & Hickl GmbH, Berlin, Germany) set to measure photon arrival times in a 25-ns window at a resolution of approximately 24 ps. This allowed the temporal pulse spread functions (TPSFs) of both laser pulses to be monitored during the experiment simultaneously [Fig. 3(b)]. The 96% output of the beamsplitter was coupled to the FT imaging gantry and focused onto the center of the gantry where the imaging specimen was placed.

Opposite the excitation source on the gantry were five detection channels separated by 22.5 deg and focused to the center of the gantry. The collected signal at each of these five positions was separated into two channels, respectively, to monitor transmitted excitation light and fluorescent light, simultaneously.[27] The filters employed in the fluorescence channels were custom-designed multiple notch filters (Chroma Technologies, Bellows Falls, Vermont) having high attenuation in 10-nm bandwidths centered at the two laser wavelengths to effectively remove excitation light from the path while allowing fluorescent light from both tracers to pass through to the TCSPC-controlled PMT detectors. The parameters of TCSPC detection of the fluorescence and transmittance TPSFs were the same as those employed for the reference PMT to allow the TPSFs from both lasers to be monitored. This allowed the temporal position of the TPSFs to be used to separate fluorescence from the different fluorophores in the imaging medium, similar to ideas presented by others.[29] The time-domain dual-wavelength data was split into separate signals by wavelength [e.g., Fig. 3(b)] and processed independently by taking the area under the TPSF from the fluorescence channel and dividing by the area under the TPSF from the transmittance channel to produce 'continuous-wave'-like Born ratio data at all source-detector pairs and for each wavelength of laser. During data collection, the laser intensity was automatically adjusted to ensure the photon detection rate was no greater than 1% of the laser pulse repetition rate (i.e., 40,000 photons/s) to avoid pulse-pile up effects. The system and all data were calibrated and Born-ratioed according to the procedures discussed in depth in another study,[28] prior to applying the dual-tracer background subtraction approach, which was followed by image reconstruction.

3.3 *Phantom Experiments*

A 30-mm diameter cylindrical polymer phantom (INO, Quebec City, Canada) was constructed with optical properties to mimic tissue at near-infrared wavelengths. At an excitation wavelength of 755 nm, the refractive index of the phantom was 1.4, $\mu_a = 0.018$ mm^{-1}, and $\mu_s' = 1.07$ mm^{-1}. The phantom was also constructed with three cylindrical inclusions running nearly the length of the phantom: one inclusion was 8 mm in diameter and the other two had a 4-mm diameter [Fig. 4(a)]. The 8-mm diameter inclusion [left hole, Fig. 4(a)] was filled with a combined 1:1 nM solution of IRDye 800CW (LI-COR Biosciences, Lincoln, Nebraska): Alexa Fluor 647 carboxylic

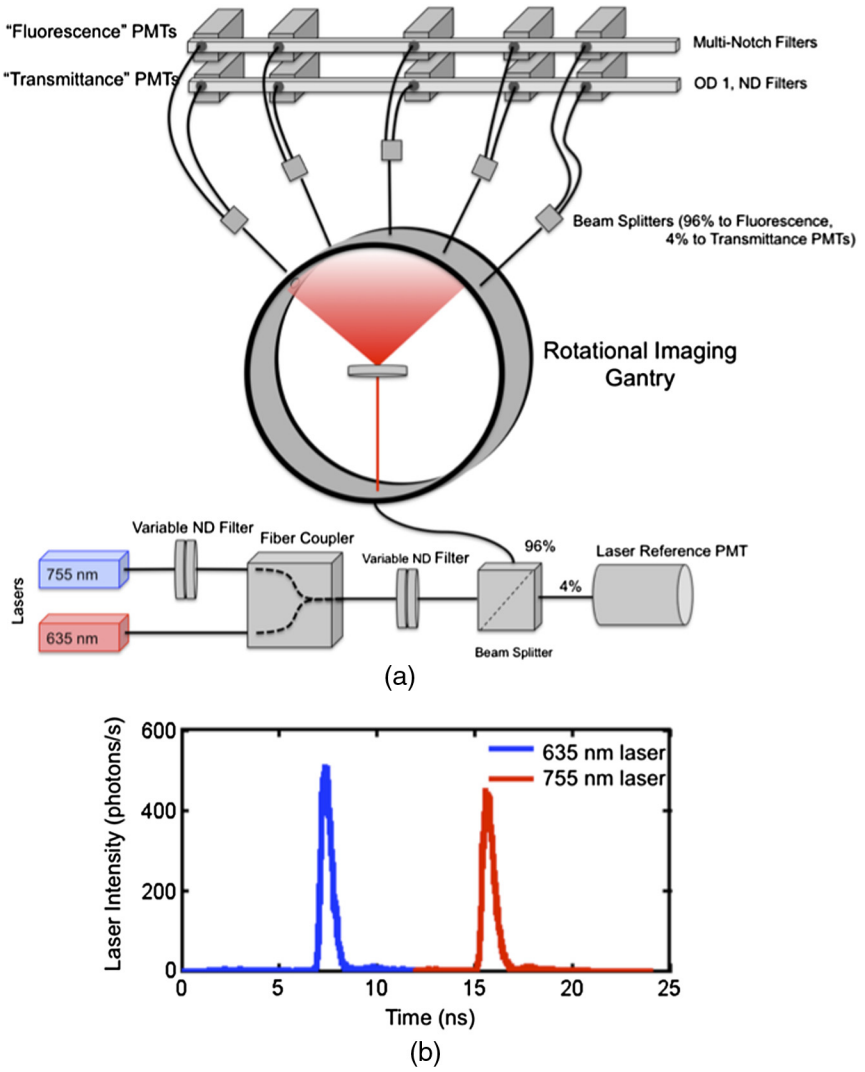

Fig. 3 A schematic of the simultaneous dual-wavelength fluorescence tomography system is presented in (a). The system is shown here in a calibration stage where the excitation light is diffused into all detection channels equally. The coupling of the lasers is depicted in the bottom portion of (a) where black lines represent fiber optic cable connections from one component of the system to the next. The rotating, non-contact imaging gantry is depicted in the middle of (a) and the detection setup is depicted above the gantry. ND represents a neutral density filter and PMT represents the photomultiplier tube detectors. An example of the simultaneous collection of the pulsed light from the two laser sources is depicted in (b), the blue data corresponds to the portion of the TPSF attributed to the 635 nm laser and the red data corresponds to that attributable to the 755-nm laser.

acid, succinimidyl ester (Life Technologies, Grand Island, New York) in 1% intralipid in water to provide a background-type inclusion characteristic of a nonspecific tracer accumulation in an organ of filtration. The Alexa Fluor 647 was mixed in water for at least 4 h prior to mixing to inactivate the ester binding site as per the manufacturer's directions. The bottom and right inclusions in Fig. 4(a) were filled with a 4:4- and an 8:4-nM ratio of the two tracers to represent an inclusion with only nonspecific uptake (equivalent uptake of targeted and untargeted tracers) and an inclusion with specific binding, respectively. The two inclusions with equivalent concentrations of targeted and untargeted tracer can also be thought of as components of a heterogeneous background in reference to the simulation studies. The phantom was then imaged on the dual-wavelength fluorescent tomography system at 64 source positions about its circumference (corresponding to 320 source-detector pairs). Data were averaged for 5 s at each source position, yielding a total scan time of 12 min. NIRFAST reconstructions were carried out on the raw Born-ratio data at the IRDye 800CW wavelength, the raw Born-ratio data at the Alexa Fluor 647 wavelength, and using the dual-tracer background subtraction approach governed by Eq. (6) where the IRDye 800CW data was substituted for d_T and the Alexa Fluor 647 data was substituted for d_U.

3.4 *Animal Experiments*

To test out the applicability of the dual-tracer background subtraction approach in an *in vivo* experiment, targeted and untargeted tracer concentrations were intravenously injected into eight athymic mice, six with human glioma tumors implanted in their left cerebral hemisphere, and two control mice. The procedure for growing the tumor is discussed in detail elsewhere.[18] The tumor line used in this study was a U251 human neuronal glioblastoma (provided by Dr. Mark Israel at Dartmouth College, Hanover, New Hampshire), which is known to overexpress the cell surface molecule, epidermal growth factor receptor (EGFR).[18] In response, an EGFR-targeted tracer, IRDye

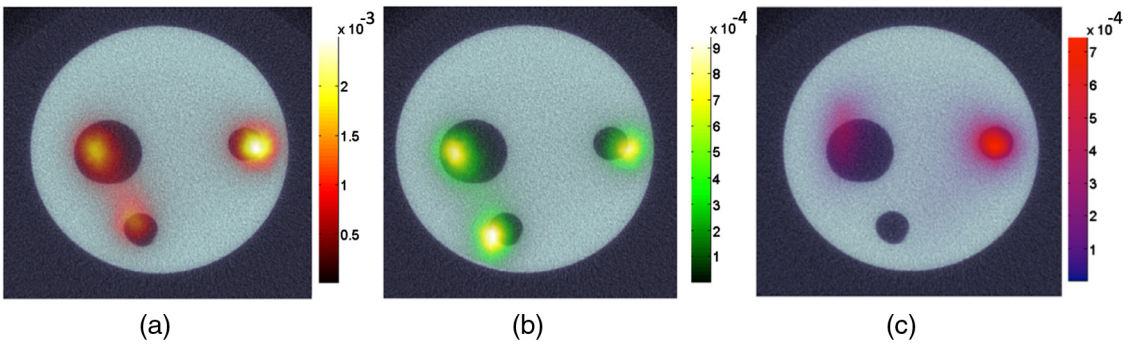

Fig. 4 Overlays of phantom optical reconstructions on x-ray CT images. Reconstruction based on only the targeted tracer excitation wavelength data is shown in (a). Reconstruction based on only the untargeted tracer excitation wavelength data is shown in (b). The dual-tracer background subtraction image based on both data sets is shown in (c).

800CW-EGF (LI-COR Biosciences, Lincoln, Nebraska) was employed and Alexa Fluor 647 was employed as the untargeted tracer. The Alexa Fluor 647 was mixed in water for at least 4 h at room temperature prior to mixing with the targeted tracer before injection to inactivate the ester binding site as per the manufacturer's directions. This is done to minimize nonspecific binding or binding to the targeted tracer. Two nmol of both tracers were injected into a tail-vein of four mice (two controls and two tumor mice). The imaging protocol and reconstructions were carried out in the same manner as described in the Methods at 4 h post tracer-injection in one tumor mouse and both controls, and at 24 h postinjection in a second tumor mouse (the mouse imaging required removal of data projections that intersected with the mouse bed).[28] The remaining four tumor mice were imaged at 1 h after injection of 0.2 nmoles of IRDye 800CW labeled anti-EGFR affibody (Affibody, Solna, Sweden) and 0.2 nmoles of Alexa Fluor 750 (Life Technologies, Grand Island, New York) labeled negative control Affibody. The labeling was done using basic maleimide chemistry as per the Affibody instruction manual. The uptake of both tracers was imaged using an eight-channel magnetic-resonance imaging-fluorescence spectroscopy system with excitation at 690 nm and spectral fluorescence detection and fitting to resolve signal from each tracer, simultaneously.[13] Contrast-enhanced magnetic resonance imaging (MRI) was carried out on all mice 1 day prior to fluorescent imaging on a Philips 3 T Achieva MRI scanner (Philips Medical Systems, Andover, Massachusetts), 10 min after injection of 100-mg/kg gadopentetate dimeglumine (Magnevist) to provide a secondary means of localizing the tumor mass, details of which have been discussed previously.[18]

4 Results and Discussion

The results from the first simulation experiment wherein background fluorescence was incrementally increased in a circular imaging domain with two circular inclusions, while keeping contrast (inclusion fluorescence minus background fluorescence) the same are presented in Fig. 1. Figure 1(bi) to 1(x) shows a reconstruction for each increase in background signal. It is clear that the quality of the fluorescence reconstruction was exceedingly sensitive to the level of background fluorescence, with substantial artifacts appearing after the third image, corresponding to a 4:1 contrast-to-background ratio (CBR). The same experiment was repeated for an order-of-magnitude higher contrast (while keeping the CBRs the same) with no observed change (results not shown). This apparent sensitivity of FT to background signal, independent of contrast, has been described previously,[6,17] and is a significant limitation to fluorescence tomography. As such, a number of efforts have been made to mitigate background effects on FT by fitting autofluorescence spectra, subtracting preinjection images from postinjection images, removing background fluorescence through analytical modeling, or constraining the reconstruction algorithms.[6,7,13,16,30,31] Figure 1(c) demonstrates the utility of a simple background subtraction technique when using the homogeneous background subtraction approach (see Sec. 3) on the data presented in Fig. 1(b). The result was that both inclusions could be seen equally well for any level of background except for in the zero-background image [(Fig. 1(ci)], where the result was worse than the corresponding naïve reconstruction in Fig. 1(bi). While the overall vast improvements in inclusion localization were obvious from comparing the background subtracted images in Fig. 1(c) with the raw-data-based images in Fig. 1(b), further discussion is warranted to explore the utility of the homogeneous background subtraction approach for *in vivo* applications.

One component of the approach is that it requires optimization of the scaling factor, c. As discussed in Sec. 2, c accounts for any scaling differences between the targeted tracer dataset and the background dataset (whether it is a forward model of homogenous background, as in this case, or the distribution of a second untargeted tracer, discussed below). This parameter is attainable only if at least one source-data projection probes an area of the imaging domain that is relatively void of bound tracer (i.e., an area inhabited by only background fluorescence signal). For most FT studies this assumption will likely hold, since in the majority of cases, targeted fluorescence is used to highlight localized pathologies in a larger field of view (such as a small tumor). One potential problem with the methodology of choosing c, however, is highlighted by the failure of the background subtraction approach when the original dataset is void of background [Fig. 1(ci)]. This failure is owed to the inherent assumption that there is at least some small level of background; therefore, in the absence of background, a small amount of the signal is still subtracted, causing fluorescence data arising from the inclusion to be removed. Furthermore the determination of c can be affected by noise in the data or spurious data collection (e.g., animal motion) if the lowest signal data projections are substantially affected. Figure 5 presents the results of an investigation into the sensitivity of the determination of c to noise in the data [Fig. 5(a)], and the effect of errors in c on the accuracy

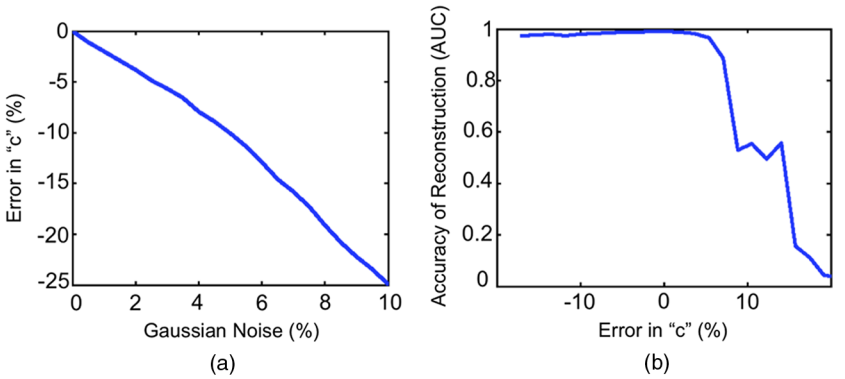

Fig. 5 The dual-tracer background subtraction approach requires a determination of the optimal scaling factor, "c", to normalize the untargeted tracer dataset to the targeted tracer dataset. The error in determining "c" based on the approach described in this paper as a function of Gaussian noise added to the raw targeted and untargeted tracer data is depicted in (a). The dependence of image reconstruction accuracy on the error in "c" is depicted in (b) where the accuracy of the reconstruction is represented by an area-under-the-curve (AUC) analysis of a receiver operating characteristic analysis for determining the location of the simulated inclusions (an AUC = 1 would be a perfect reconstruction).

of dual-tracer image reconstruction [Fig. 5(b)]. Figure 5(a) demonstrates that c will tend to be underestimated in the presence of Gaussian noise up to 10% added to the simulated targeted and untargeted data from the Fig. 1(bx) simulation, and Fig. 5(b) suggests that an underestimation in c will cause less reconstruction errors than an overestimation in c. This is likely a result of problems associated with dealing with negative data vectors in the image reconstruction.

Another important component of the homogeneous background subtraction approach is the assumption that the background is homogeneous. If indeed the background fluorescence is homogenous, this approach is powerful since it is not specific to any imaging geometry and does not require a second tracer to be injected; however, the nature of *in vivo* background fluorescence may be more complex. Background fluorescence in the context of systemically injected targeted fluorescent tracers is comprised of two constituents, nonspecific fluorophore uptake (i.e., fluorescence arising from fluorescent tracer concentrations that are not bound to the specific target of interest), and autofluorescence (i.e., fluorescence arising from endogenous fluorophores). While autofluorescence is a major problem in the visible spectrum,[32] it becomes much less of an effect in the near-infrared wavelength range (600 to 1000 nm), where many new tracers are being developed to exploit this property, as well as relatively low absorption properties. In fact, within the near-infrared spectrum, it is much more likely that the background fluorescence signal is predominantly comprised of nonspecific tracer uptake.[3] While this fact means that the nonspecific tracer uptake autofluorescence assumption made to derive Eq. (6) is adequate, heterogeneities in biological tissue with respect to blood flow and vascular permeability mean that *in vivo* background fluorescence is likely quite heterogeneous.

To test out the effect a heterogeneous background could have on the homogeneous background subtraction approach used in Fig. 1, another set of simulated data were created on the fluorescent mesh depicted in Fig. 2(a). Figure 2(c) demonstrates that the effect of the variable background renders it impossible for raw fluorescent data to be used to reconstruct the location of the inclusions of interest. This is not unexpected, as a more rigorous examination of the effects of fluorescence heterogeneity on FT demonstrated that reconstructions can be affected by heterogeneous background when the tumor-to-background contrast is less than 100:1.[33] Likewise, even the homogeneous background subtraction method was not optimal in the face of the heterogeneous background [Fig. 2(d)]. However, when a distribution of a second, untargeted tracer was simulated [Fig. 2(b)], matching the variable background of the simulated targeted tracer distribution, the dual-tracer background subtraction approach (see Sec. 2) was capable of effectively removing the variable background, making the bound fluorescent tracer inclusions visible [Fig. 2(e)]. It should be noted that in this simulation, 10% differences in optical properties were used to create the targeted and untargeted tracer datasets, respectively, suggesting that the proposed dual-tracer background subtraction approach is insensitive to differences in optical properties at the necessarily different wavelengths needed to resolve two tracers, simultaneously. Furthermore, there will always be errors associated with estimates of optical properties for any given

Table 1 Tumor contrast achievable by reconstruction of the targeted-tracer uptake, the untargeted-tracer uptake, and the dual-tracer reconstruction for all mice expressed in terms of contrast-to-background ratios (CBRs), which are (mean tumor signal-mean background signal)/mean background signal. Each mouse is labeled by the time in hours after tracer injection the imaging was carried out. The numbers in parentheses separate images taken at the same time point.

Mouse	Targeted tracer CBR	Untargeted tracer CBR	Dual-tracer CBR
1 h (1)[a]	−0.57	−0.70	1.83
1 h (2)	−0.33	−0.42	1.26
1 h (3)	−0.59	−0.73	0.69
1 h (4)	−0.36	−0.43	0.66
4 h[a]	0.01	−0.13	4.97
24 h[a]	4.36	2.75	7.21
1 h Control (1)[a]	−0.53	−0.34	−0.02
1 h Control (2)	−0.61	−0.44	−0.09

[a]Imaging results are presented in Fig. 6

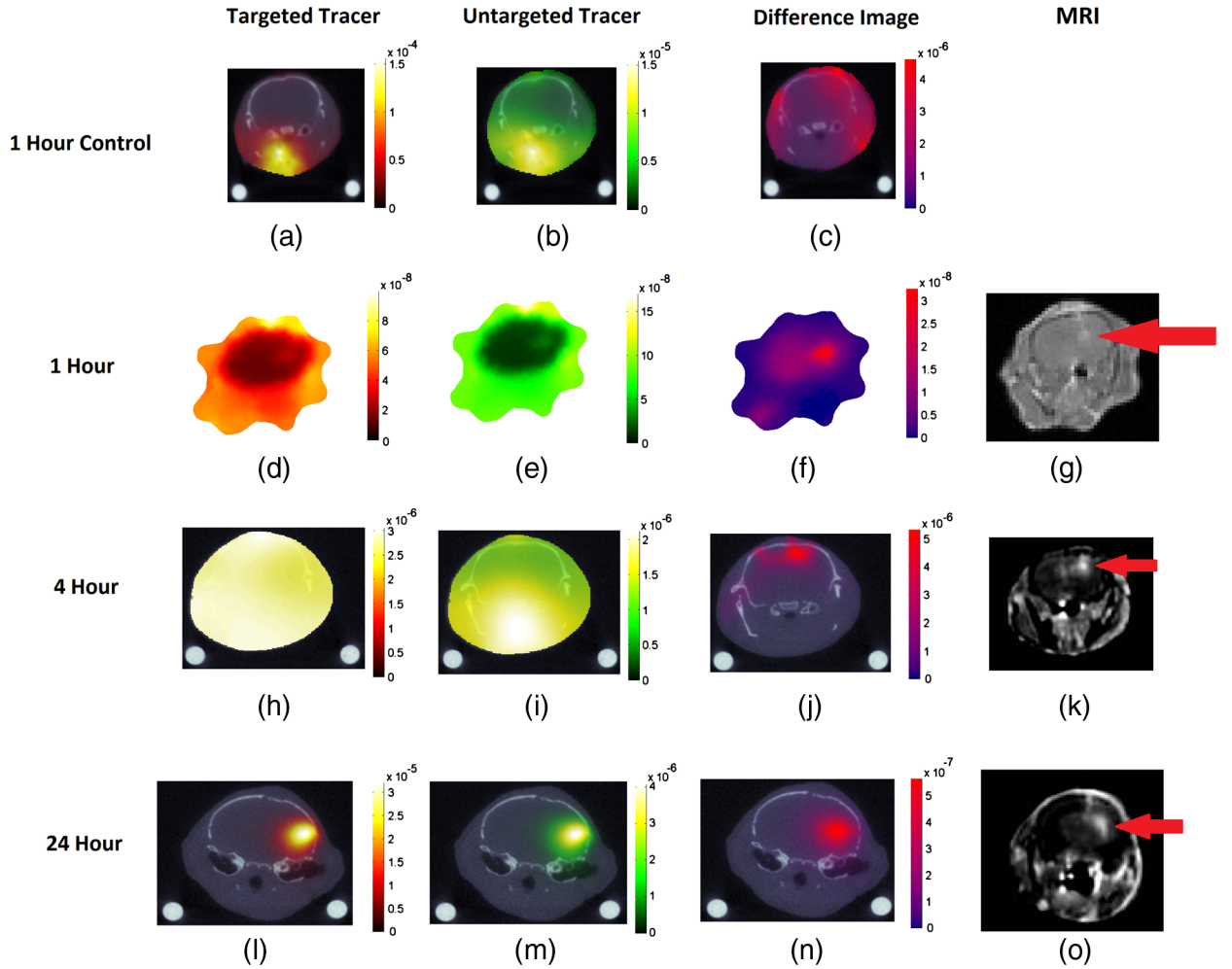

Fig. 6 Overlays of *in vivo* optical reconstructions on x-ray CT images are shown in (a)–(c) for a control mouse at 1 h after dual-tracer injection, in (d)–(f) for a tumor mouse at 1 h postinjection, in (h)–(j) for the tumor mouse at 4 h postinjection, and in (l-n) for the tumor mouse at 24 h postinjection. Reconstruction based on only the targeted tracer excitation wavelength data is shown in (a), (d), (h), and (l), reconstruction based on only the untargeted tracer excitation wavelength data is shown in (b), (e), (i), and (m), and the dual-tracer background subtraction image is shown in (c), (f), (j), and (n). Contrast-enhanced MRI shows the location of the glioma in the corresponding tumor mice (g), (k), and (o).

imaging domain; however, the results of this simulation take this possible error into account as well, suggesting that the 'best guess' forward model matrix introduced in Eq. (5) is likely to be sufficient to reconstruct either tracer at its wavelength, independently, given that a Born ratio formulation would be used to suppress model error.

The results of the phantom study presented in Fig. 4 provide experimental support for the utility of the dual-tracer background subtraction approach. The phantom consisted of three inclusions with the largest used as an estimation of a background level with low and equal concentration of targeted and untargeted tracer, a second inclusion was an estimation of an organ of filtration with high, but also equal, concentrations of both tracers, and the third inclusion was an estimation of a target of interest, such as a tumor, with a very high concentration of targeted tracer and a high concentration of untargeted tracer. The high concentration of untargeted tracer would be expected in tumors because of the enhanced permeability and retention effect.[34] The reconstructions of the targeted and untargeted tracer datasets on their own are presented in Fig. 4(a) and 4(b), respectively. In both cases, all three inclusions were visible, which is not surprising since the background fluorescence of the phantom is negligible and therefore approximates the infinite contrast scenario in Fig. 1(ai). However, looking at the targeted fluorescence distribution in Fig. 4(a), it is not clear which of the inclusions is the 'tumor' inclusion. Only by applying the dual-tracer background subtraction approach, the reconstruction of which is shown in Fig. 4(c), could the 'tumor' inclusion clearly be realized. This demonstrates the ability of the approach to be used to remove heterogeneous background and large nonspecific uptake, such as might be expected in organs of filtration (e.g., the liver or kidneys). A postreconstruction difference image of Fig. 4(a) and 4(b) was carried out to compare to the result in Fig. 4(c), but no scaling value could be found that did not result in significant edge artifacts (results not shown). This highlights the importance of carrying out the dual-tracer data differencing prior to reconstruction as opposed to after reconstructing both tracer distributions, independently.

The results of the mouse imaging experiments are presented in Table 1 and Fig. 6. Table 1 presents the results from image reconstructions of targeted tracer uptake, untargeted tracer uptake, and the dual-tracer approach for all mice in terms of ability to localize the tumor (or in the case of the controls: an arbitrary region of the brain) assessed by contrast-to-background ratio

[CBR: (mean tumor signal—mean background signal)/background signal]. The table demonstrates that up to 4 h after the injection the contrast in the tumor of either targeted or untargeted tracer was negative (i.e., there was more nonspecific uptake of the tracers in the tissue surrounding the tumor (brain and head) than in the brain). However, the dual-tracer background subtraction approach, which is sensitive to bound fractions of the targeted tracer, demonstrated clear tumor contrast in all mice even at the early 1 h postinjection time-points. The contrast-to-background ratio in the tumor tended to increase with time from an average of 1.11 ± 0.55 at 1 h to almost five at 4 h and upwards of seven at 24 h postinjection, suggesting a greater abundance of binding with increased time, which is expected for this U251 tumor line.[20,35] Reconstructed images of the 24-h, 4-h, 1-h, and one of the 1-h control mice are presented in Fig. 6. It warrants noting that by the 24-h point it was possible to accurately resolve the tumor using either the targeted tracer or the untargeted tracer uptake image reconstructions, as well as the dual-tracer image, as each demonstrated a high tumor CBR. The fact that the untargeted tracer also located to the tumor suggests a considerable amount of nonspecific uptake in the tumor owing to enhanced vascular permeability and retention effects.[34] This further suggests that a significant portion of the targeted tracer uptake in the tumor may come from unbound signal, highlighting the use of the secondary tracer to make more quantitative assessments of tracer-binding and receptor abundance, even at late time-points after injection. Results from the two control mice imaged at 1 h after injection demonstrated some accumulation of targeted and untargeted tracer concentration in the tissue below the skull, which is where the carotid arteries and other large blood vessels can be found, while the dual-tracer reconstructions demonstrated relatively homogenous distributions.

It should be noted that the success of the dual-tracer background subtraction methodology presented in this study is

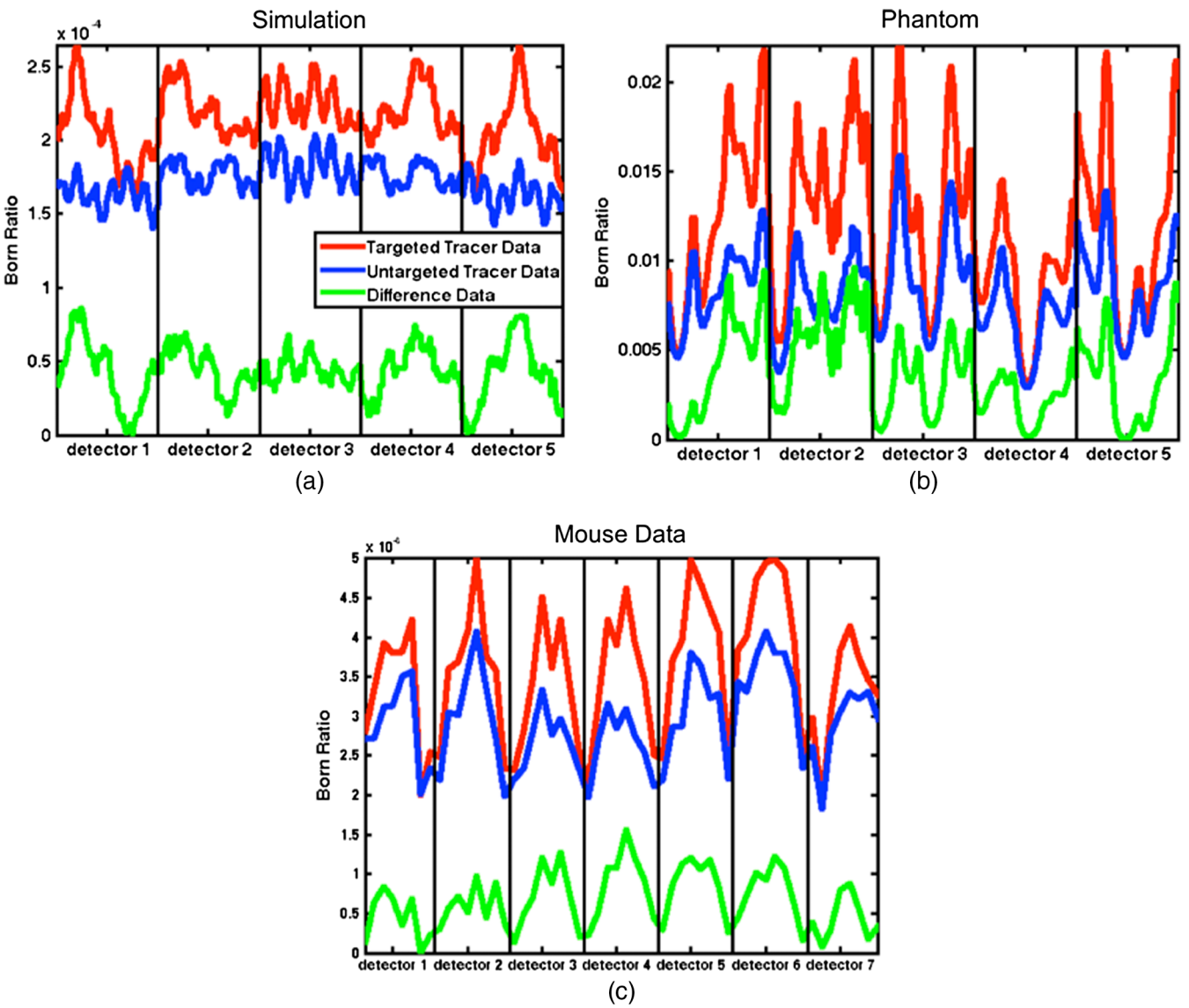

Fig. 7 Born ratio data (fluorescence/transmittance) for the heterogeneous background simulated dataset, the phantom dataset, and a 1 h postinjection mouse dataset are presented in (a)–(c), respectively. The red data represents the Born ratio as a function of source-detector pair number for the targeted tracer data, the blue data represents the same thing for the corrected untargeted tracer data (i.e., cd_U), and the green data represents the subtraction of the untargeted dataset from the targeted dataset (i.e., red minus blue). The data are arranged that all projections from a single detector are combined in columns separated by the vertical black lines. The number of detectors is higher in (c) than in (a) and (b) because this data set was collected with a different fluorescence tomography system (see Sec. 3).

highly dependent on the selection of a suitable targeted/untargeted tracer pair. Both tracers must have similar transport kinetics (i.e., vascular permeability), similar plasma pharmacokinetics (i.e., be metabolized similarly), and similar levels of nonspecific uptake and binding. While the IRDye 800CW-EGF is significantly larger than Alexa Fluor (~7 versus. 1.3 kDa), all of these listed factors have been demonstrated to be approximately equivalent for another similar tracer pairing: IRDye 800CW-EGF and untargeted IRDye 700DX.[20,35–38] The choice of Alexa Fluor 647 as an untargeted tracer in the current study to replace IRDye 700DX was based on the wavelength requirements of the FT system employed and the fact that the tracer has a similar size to IRDye 700DX (1.3 versus 1.9 kDa), both being known for having low nonspecific binding. While a more rigorous study is needed to determine the extent of suitability of Alexa Fluor 647 to be used as an untargeted tracer for IRDye 800CW-EGF, the simulation and phantom results presented in this study do not rely on this suitability and the *in vivo* results of the present study suggest that its employment can help improve tumor contrast in FT at early time-points after tracer injection. Despite this, before employing a dual-tracer background subtraction, the suitability of the targeted/untargeted tracer should be evaluated on a case-by-case basis. Furthermore, future studies using this dual-tracer background subtraction algorithm could investigate the use of more sophisticated single-targeted molecules with two fluorescent molecules, one that would activate upon binding and one always active as presented by Chen et al.,[39] as a means of avoiding the need to choose a suitable tracer pairing, thus avoiding problems of differential uptake between the tracers.

5 Conclusions

A potential procedure for accurate background subtraction was presented to improve targeted-tracer fluorescence molecular tomography. Essentially, tomographic signal from the uptake of a second untargeted tracer is used to subtract off the component of the targeted tracer signal that arose from nonspecific uptake [see example of raw data subtractions in Fig. 7 for simulation (a), a phantom study (b), and a mouse experiment (c)]. Support has been shown in multiple simulations, a phantom study, and in a orthotopic glioma mouse model. These tests demonstrate the ability of this methodology to allow recovery of contrast that would be unrecoverable with conventional FT. The peripheral benefit of this approach is that there are few time constraints on when this type of imaging can be done *in vivo*, opening up a range of applications in molecular imaging that would be otherwise unattainable.

Acknowledgments

This work was funded by NCI grants R01CA120368, R01CA109558, and K25 CA138578. KMT acknowledges funding from a CIHR fellowship.

References

1. V. Ntziachristos et al., "Looking and listening to light: the evolution of whole-body photonic imaging," *Nat. Biotechnol.* **23**(3), 313–320 (2005).
2. F. Leblond et al., "Pre-clinical whole-body fluorescence imaging: review of instruments, methods and applications," *J. Photochem. Photobiol. B* **98**(1), 77–94 (2010).
3. J. L. Kovar et al., "A systematic approach to the development of fluorescent contrast agents for optical imaging of mouse cancer models," *Anal. Biochem.* **367**(1), 1–12 (2007).
4. E. Nordberg et al., "Cellular studies of binding, internalization and retention of a radiolabeled EGFR-binding affibody molecule," *Nucl. Med. Biol.* **34**(6), 609–618 (2007).
5. Z. Zhang et al., "Monomolecular multimodal fluorescence-radioisotope imaging agents," *Bioconjugate Chem.* **16**(5), 1232–1239 (2005).
6. M. Gao et al., "Effects of background fluorescence in fluorescence molecular tomography," *Appl. Opt.* **44**(26), 5468–5474 (2005).
7. J. Chang, H. L. Graber, and R. L. Barbour, "Improved reconstruction algorithm for luminescence optical tomography when background lumiphore is present," *Appl. Opt.* **37**(16), 3547–3552 (1998).
8. M. J. Eppstein et al., "Three-dimensional, Bayesian image reconstruction from sparse and noisy data sets: near-infrared fluorescence tomography," *Proc. Natl. Acad. Sci. U. S. A.* **99**(15), 9619–9624 (2002).
9. A. B. Milstein et al., "Fluorescence optical diffusion tomography," *Appl. Opt.* **42**(16), 3081–3094 (2003).
10. R. Roy and E. Sevick-Muraca, "Truncated Newton's optimization scheme for absorption and fluorescence optical tomography: part II Reconstruction from synthetic measurements," *Opt. Express* **4**(10), 372–382 (1999).
11. R. Roy and E. Sevick-Muraca, "Truncated Newton's optimization scheme for absorption and fluorescence optical tomography: part I theory and formulation," *Opt. Express* **4**(10), 353–371 (1999).
12. A. Corlu et al., "Three-dimensional *in vivo* fluorescence diffuse optical tomography of breast cancer in humans," *Opt. Express* **15**(11), 6696–6716 (2007).
13. S. C. Davis et al., "Magnetic resonance-coupled fluorescence tomography scanner for molecular imaging of tissue," *Rev. Sci. Instrum.* **79**(6), 064302 (2008).
14. P. B. Jones et al., "Two postprocessing techniques for the elimination of background autofluorescence for fluorescence lifetime imaging microscopy," *J. Biomed. Opt.* **13**(1), 014008 (2008).
15. F. C. Piccolino et al., "Pre-injection fluorescence in indocyanine green angiography," *Ophthalmology.* **103**(11), 1837–1845 (1996).
16. F. Liu et al., "Extraction of target fluorescence signal from *in vivo* background signal using image subtraction algorithm," *Int. J. Autom. Comput.* **9**(3), 232–236 (2012).
17. A. Soubret and V. Ntziachristos, "Fluorescence molecular tomography in the presence of background fluorescence," *Phys. Med. Biol.* **51**(16), 3983–4001 (2006).
18. S. L. Gibbs-Strauss et al., "Detecting epidermal growth factor receptor tumor activity *in vivo* during cetuximab therapy of murine gliomas," *Acad. Radiol.* **17**(1), 7–17 (2010).
19. K. S. Samkoe et al., "Imaging tumor variation in response to photodynamic therapy in pancreatic cancer xenograft models," *Int. J. Radiat. Oncol. Biol. Phys.* **76**(1), 251–259 (2010).
20. K. M. Tichauer et al., "Improved tumor contrast achieved by single time point dual-reporter fluorescence imaging," *J. Biomed. Opt.* **17**(6), 066001 (2012).
21. K. M. Tichauer et al., "Computed tomography-guided time-domain diffuse fluorescence tomography in small animals for localization of cancer biomarkers," *J. Vis. Exp.* (65) e4050 (2012).
22. E. M. Sevick-Muraca and C. L. Burch, "Origin of phosphorescence signals reemitted from tissues," *Opt. Lett.* **19**(23), 1928–1930 (1994).
23. V. Ntziachristos and R. Weissleder, "Experimental three-dimensional fluorescence reconstruction of diffuse media by use of a normalized Born approximation," *Opt. Lett.* **26**(12), 893–895 (2001).
24. S. R. Arridge, "Optical tomography in medical imaging," *Inverse Probl.* **15**(2), R41–R93 (1999).
25. G. A. Wagnieres, W. M. Star, and B. C. Wilson, "*In vivo* fluorescence spectroscopy and imaging for oncological applications," *Photochem. Photobiol.* **68**(5), 603–632 (1998).
26. H. Dehghani et al., "Near infrared optical tomography using NIRFAST: algorithm for numerical model and image reconstruction," *Commun. Numer. Meth. Eng.* **25**(6), 711–732 (2009).
27. D. Kepshire et al., "A microcomputed tomography guided fluorescence tomography system for small animal molecular imaging," *Rev. Sci. Instrum.* **80**(4), 043701 (2009).

28. K. M. Tichauer et al., "Imaging workflow and calibration for CT-guided time-domain fluorescence tomography," *Biomed. Opt. Express* **2**(11), 3021–3036 (2011).
29. V. Ntziachristos et al., "Multichannel photon counting instrument for spatially resolved near infrared spectroscopy," *Rev. Sci. Instrum.* **70**(1), 193–201 (1999).
30. J. R. Mansfield et al., "Autofluorescence removal, multiplexing, and automated analysis methods for *in-vivo* fluorescence imaging," *J. Biomed. Opt.* **10**(4), 041207 (2005).
31. A. Soubret, J. Ripoll, and V. Ntziachristos, "Accuracy of fluorescent tomography in the presence of heterogeneities: study of the normalized born ratio," *IEEE Trans. Med. Imag.* **24**(10), 1377–1386 (2005).
32. A. Garofalakis et al., "Three-dimensional *in vivo* imaging of green fluorescent protein-expressing T cells in mice with noncontact fluorescence molecular tomography," *Mol. Imag.* **6**(2), 96–107 (2007).
33. A. K. Sahu et al., "Evaluation of anatomical structure and non-uniform distribution of imaging agent in near-infrared fluorescence-enhanced optical tomography," *Opt. Express* **13**(25), 10182–10199 (2005).
34. H. Maeda et al., "Tumor vascular permeability and the EPR effect in macromolecular therapeutics: a review," *J. Control. Release.* **65**(1–2) 271–284 (2000).
35. K. M. Tichauer et al., "*In vivo* quantification of tumor receptor binding potential with dual-reporter molecular imaging," *Mol. Imag. Biol.* **14**(5), 584–592 (2012).
36. K. S. Samkoe et al., "High vascular delivery of egf, but low receptor binding rate is observed in AsPC-1 tumors as compared to normal pancreas," *Mol. Imag. Biol.* **14**(4), 472–479 (2012).
37. K. M. Tichauer et al., "Advantages of a dual-tracer model over reference tissue models for binding potential measurement in tumors," *Phys. Med. Biol.* **57**(20), 6647–6659 (2012).
38. B. W. Pogue et al., "Imaging targeted-agent binding *in vivo* with two probes," *J. Biomed. Opt.* **15**(3), 030513 (2010).
39. A. K. Chen et al., "Ratiometric bimolecular beacons for the sensitive detection of RNA in single living cells," *Nucleic Acids Res.* **38**(14), e148 (2010).